Short Communication

GREENHOUSE GASES SCIENCE AND TECHNOLOGY

Effect of the intermediate principal stress on the evolution of mudstone permeability under true triaxial compression

Lu Shi, Zhijiao Zeng, Bing Bai and Xiaochun Li, State Key Laboratory of Geomechanics and Geotechnical Engineering, Institute of Rock and Soil Mechanics, Chinese Academy of Sciences, Wuhan, China

Abstract: The changes in the permeability of mudstone specimens under compression with different intermediate principal stresses (σ_2) were tested using a true triaxial testing system. The confining pressure and pore pressure were set based on the caprock conditions in a CO_2 geological storage project. The measured permeability initially increased and then decreased before the failure of the specimen and reached a peak in the form of a sudden increase during the formation of the fault. The permeability during compression decreased with increasing σ_2. However, the higher σ_2 caused the ductility of the mudstone to decrease significantly and led to the formation of a fault parallel to the σ_2 direction. The increase in permeability during the formation of the fault was notably suppressed by the increase in the confining pressure and decreased with increasing flatness of the fault; the flatness of the fault increased with increasing σ_2. Moreover, an empirical function that considers the compressive and dilatant strains was proposed to predict the permeability before the failure of the specimen, and the parameters of this function are only slightly affected by σ_2. The results of this study reveal the effect of σ_2 on the variation of the permeability of mudstone and help better assess the risk of caprock leakage in injection projects. © 2017 Society of Chemical Industry and John Wiley & Sons, Ltd.

Keywords: true triaxial testing; mudstone; intermediate principal stress; permeability; ductility

Introduction

CO_2 capture and geological storage (CCS) is a key technology in reducing CO_2 emissions, which has been of great concern for many countries.[1–4] The purpose of implementing CO_2 geological storage is to safely isolate CO_2 for long periods of time in rock formations deep in the crust, particularly deep saline aquifers.[5–7] The effectiveness and safety of CCS projects depend primarily on the sealing and integrity of the caprock, and the permeability of the caprock is an important factor affecting its sealing performance.[8,9] The injection of fluid causes the pressure in the reservoir to change, and the stress field of the caprock is disturbed, which may lead to the deformation and failure of the caprock material and, thus, a change in the permeability of the caprock. Thus, the change in the permeability of the

Correspondence to: Lu Shi, State Key Laboratory of Geomechanics and Geotechnical Engineering, Institute of Rock and Soil Mechanics, Chinese Academy of Sciences, Wuhan 430071, China
E-mail: shilu.whrsm@qq.com
Received May 26, 2017; revised August 2, 2017; accepted September 12, 2017
Published online at Wiley Online Library (wileyonlinelibrary.com). DOI: 10.1002/ghg.1732

caprock due to the stress disturbance can affect the leakage risk of the CCS site.

Many experimental studies have focused on the changes in permeability under compressive stress.[10–15] The evolution of rock permeability typically includes three stages: it decreases slightly in the elastic stage; after entering the plastic stage, it increases at an increasing rate and reaches the peak after failure; and with increasing strain, the permeability may continue to increase or may decrease gently or drastically. During this process, the increase in rock permeability and the variation in the post-failure stage are closely related to the type of rock and the confining pressure.[11,15] The caprocks of many CCS projects, such as the Sleipner Project Norway,[16] the Otway Pilot Project in Australia,[17] the In Salah project in Algeria,[18] and the Shenhua CCS demonstration project in China,[19] are mainly composed of mudstone. Because the caprock is typically buried at a depth of 1 km or more, the hydrostatic pressure is close to or greater than 30 MPa. Under such high confining pressures, mudstone can exhibit ductile behavior, and even if shear failure occurs, the compacting shear fractures will remain closed and sealing,[20] which is highly beneficial to the safety of a CCS project.

The results described above were obtained under conventional triaxial compression, in which the stress path is limited to the plane on which $\sigma_2 = \sigma_3$. However, the rocks in the crust are typically subjected to a general stress state in which $\sigma_1 > \sigma_2 > \sigma_3$ (where σ_1, σ_2 and σ_3 are the principal stresses).[21–24] The intermediate principal stress σ_2 has been shown to have a significant effect on the strength and deformation properties of rocks, and the ductility of rocks can be decreased by increasing σ_2.[25–27] However, other than Takahashi *et al.*,[28] Al-Harthy *et al.*,[29] and Li,[11] who studied the permeability characteristics of sandstone in true triaxial stress environments, few studies have investigated the influence of σ_2 on the permeability of mudstone. In this work, the permeability of mudstone in a complete stress-strain process is tested under different σ_2 conditions using a true triaxial testing system, and the impact of σ_2 on the permeability evolution characteristics of mudstone during compression is discussed. The mudstone is compressed under a relatively high confining pressure because of the significant burial depths in CCS projects. The results reveal that σ_2 plays an important role in the variation of the permeability of mudstone under compressive stress conditions and help better assess the leakage risk of the caprock in injection projects.

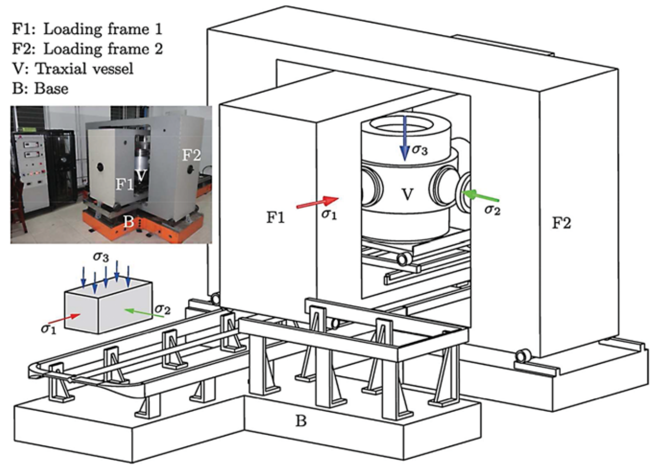

Figure 1. Schematic diagram of the RT3-II true triaxial apparatus developed at the Institute of Rock and Soil Mechanics, Chinese Academy of Sciences.

Experimental set-up

The mechanical and permeability tests were conducted at the Institute of Rock and Soil Mechanics, Chinese Academy of Sciences (WHRSM) with the RT3-II true triaxial apparatus (TTA) for rocks.[30–32] This apparatus consists of four subsystems: three subsystems for loading the maximum principal stress, intermediate principal stress and confining pressure and one subsystem for measuring the permeability (Figs 1 and 2). Therefore, the TTA can exert loads on a specimen in three directions independently and precisely using servos. Compared to the original TTA designed by Mogi,[26] the distinctive features of the TTA are the designs of two moveable loading frames in a horizontal layout, multi-level tracks and the specimen-centering device, which improve the apparatus considerably in terms of its operability, loading capacity, ability to capture the complete stress-strain curve of rocks and suppression of off-center loading.

The RT3-II TTA can accommodate a rectangular prismatic specimen with a size of 50 × 50 × 100 mm and provide stresses of up to 1000 MPa in both the σ_1 and σ_2 directions by the loading frames and a confining pressure of up to 100 MPa by a triaxial vessel. Moreover, the maximum confining pressure allows for a pore pressure of up to 50 MPa without bypass flow in the permeability tests. The three strains of the specimen are measured by three linear variable

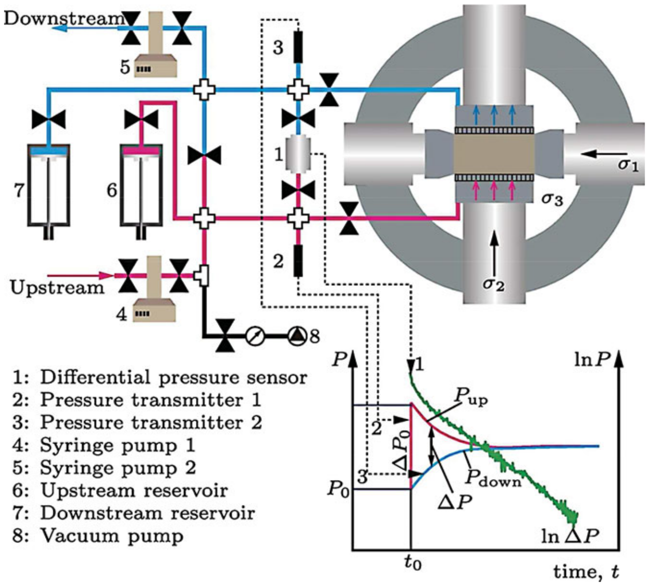

Figure 2. Schematic diagram of the permeability measurement subsystem.

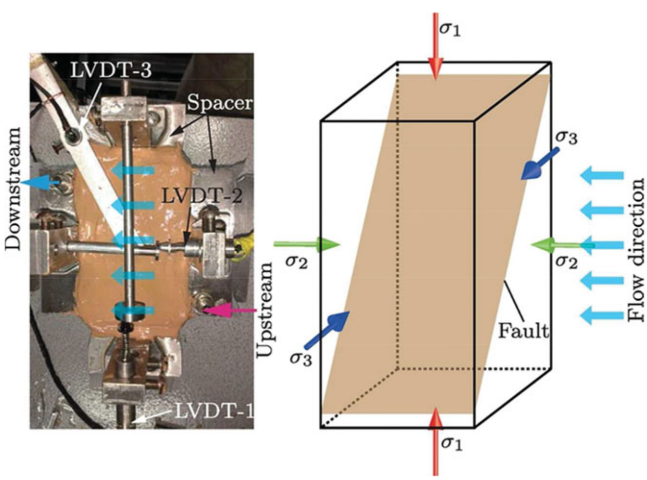

Figure 3. Orientation of the faults and direction of the fluid flow in the true triaxial tests.

differential transformers (LVDTs) with nominal ranges of ±6.5, ±2.5, and ±2.5 cm in the σ_1, σ_2 and σ_3 directions, respectively, which are represented by ε_1, ε_2, and ε_3, respectively (Fig. 3).

The subsystem for measuring the permeability (Fig. 2) was modified from TPM-6 permeability measurement equipment[33–35] and can be divided into upstream and downstream parts. A syringe pump (100DX from TELEDYNE ISCO) is connected at the end of each part to provide a constant flow with a range of 0.01 μL/min to 50 mL/min or a constant pressure of 0 to 68.95 MPa. The other end of each part is connected to a pair of faces of the specimen in the σ_1 or σ_2 direction. Two pressure transmitters (Y91 from Baumer) with a range of 0–40 MPa are mounted to measure the upstream and downstream pressures. Although the constant flow method and constant pressure method can be used, the TPM-6 was designed to measure the permeability of a specimen rapidly with the transient pulse method proposed by Brace *et al.*,[36] in which a sudden pressure increment ΔP_0 occurs in the upstream part. The decay in the differential pressure ΔP between the upstream pressure P_{up} and downstream pressure P_{down} for gas can be expressed as[37]

$$\ln \frac{\Delta P}{\Delta P_0} = m_1 t \qquad (1)$$

with

$$m_1 = -\frac{f_1 A P_m k}{14696 \mu_g L f_z}\left(\frac{1}{V_1} + \frac{1}{V_2}\right)$$

where A and L are the cross-sectional area and length of the specimen in the flow direction, respectively; k is the permeability; μ_g is the gas viscosity; P_m is the mean absolute pressure; f_1 and f_z are correction factors associated with the mass flow and gas compressibility, respectively; and V_1 and V_2 are the upstream and downstream reservoir volumes, respectively.

The differential pressure between the upstream and downstream parts, which is typically considerably smaller than the pore pressure, is important for obtaining the permeability of a specimen according to Eqn (1). Thus, a differential pressure sensor (Validyne Engineering) with a full scale of 220 kPa is necessary to monitor ΔP precisely. Additionally, a storage-variable reservoir (0.1–1000 mL) is connected to each part to adjust the decay rate of ΔP, which increases the permeability measurement range.

Specimens and test procedure

Specimens

Mudstone drilled from Yingcheng, Hubei Province, China, was selected for this study. The brown mudstone is from Eocene strata. The cores were sealed using wax immediately after drill-out. All the cores were polished into cuboid-shaped specimens with sizes of 50 × 50 × 100 mm. The specimens were dried at a temperature of 333 K to a constant weight and then wrapped with preserving film.

The pore size distribution of the mudstone (Fig. 4), which was measured using a mercury porosimeter,

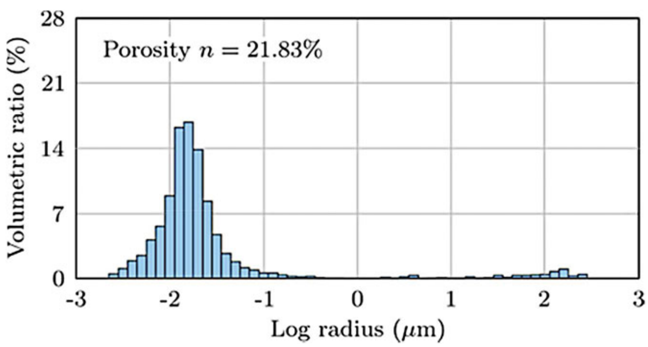

Figure 4. Pore size distribution of the Yingcheng mudstone from mercury porosimetry.

shows that pores with a radius of 16 nm are most abundant and that pores with a radius less than approximately 0.1 μm account for more than 95% of the total porosity. The pores in this rock are considerably smaller than those in clastic sandstone. However, the porosity of the mudstone reaches 21.83%, which indicates that the diagenetic depth is relatively shallow. The uniaxial compressive strength of the mudstone is approximately 35 MPa.

Experimental scheme

Four specimens from the same round trip were compressed at different σ_2 values to study the impact of σ_2 on the evolution of mudstone permeability during the complete stress-strain process. During the compression, the confining pressure and pore pressure P_0 were held at 35 and 15 MPa, respectively, which are similar to the conditions of the first reservoir in the Shenhua CCS project.[19] In addition, based on the measured geostress data in mainland China collected by Jing *et al.*,[24] the upper bound of σ_2 is 60 MPa, which corresponds to crustal stress conditions at a depth of 3000 m. Thus, the intermediate principal stresses during the compression of these specimens, which were called P15, P11, P14, and P16, were maintained at 36, 41, 50, and 60 MPa, respectively. Note that σ_2 must greater than σ_3 to normalize the deformation measurements. Therefore, the initial value of σ_2 was set to 36 MPa to approximate the conventional triaxial compression state. To determine the evolution of the permeability at low confining pressures, the permeability of another specimen, P4, was also measured with compression at $\sigma_2 = 10$ MPa, $\sigma_3 = 8$ MPa and $P_0 = 5$ MPa. The pore fluid was nitrogen, and the system temperature in the tests was 303 K.

The permeability may become anisotropic under true triaxial stresses, even in an isotropic material.[11,28] However, it is difficult to measure the permeability in every direction of the specimen during compression. Numerous test results show that a rock specimen fails with a fault forming parallel to σ_2,[25–27] which means that the fluid flowing in the direction of σ_2 in the post-peak region can still be approximated as a one-dimensional problem. However, if fluid flows in the σ_1 direction, the three-dimensional flow will hinder the interpretation of the results. In addition, when the fault does not pass through the σ_1 surfaces, as shown in Fig. 3, measuring the permeability in the σ_1 direction will considerably underestimate the effect of the fault on the permeability. In this study, the setting of the apparatus and the connection of the pipe enabled us to measure the permeability in the σ_2 direction (Figs 2 and 3). Therefore, 112 flow-guiding holes with diameters of 1 mm were evenly distributed on each steel spacer of σ_2 such that the fluid was uniformly distributed on the σ_2 surfaces.

Moreover, because the permeability of mudstone is relatively low, the reservoirs were closed to making the storage upstream and downstream approximately 28 mL and 22 mL, respectively.

Experimental procedure

The procedure for measuring the permeability of mudstone under true triaxial compressive conditions includes five steps.

(1) Specimen mounting

The specimen and two pairs of steel spacers were assembled precisely with a specially designed jig. Polyurethane was painted on the assembly. After the polyurethane had cured, a coating (Fig. 3) formed to isolate the specimen from the hydraulic oil inside the triaxial vessel. The assembly and the LVDT-based strain transducers were placed on the specimen-centering device of the triaxial vessel. The position of the specimen could then be adjusted to align with the loading pistons of the triaxial vessel in the horizontal and vertical directions.

(2) Pre-loading

After closing the triaxial vessel, the TTA was turned into the experimental state along the tracks shown in Fig. 1. Pre-loadings of 4 MPa and 2 MPa in the σ_1 and σ_2 directions, respectively, were used to clamp the specimen and spacer assembly. Therefore, the

  | *Greenhouse Gas Sci Technol*. **8**:37–50 (2018); DOI: 10.1002/ghg

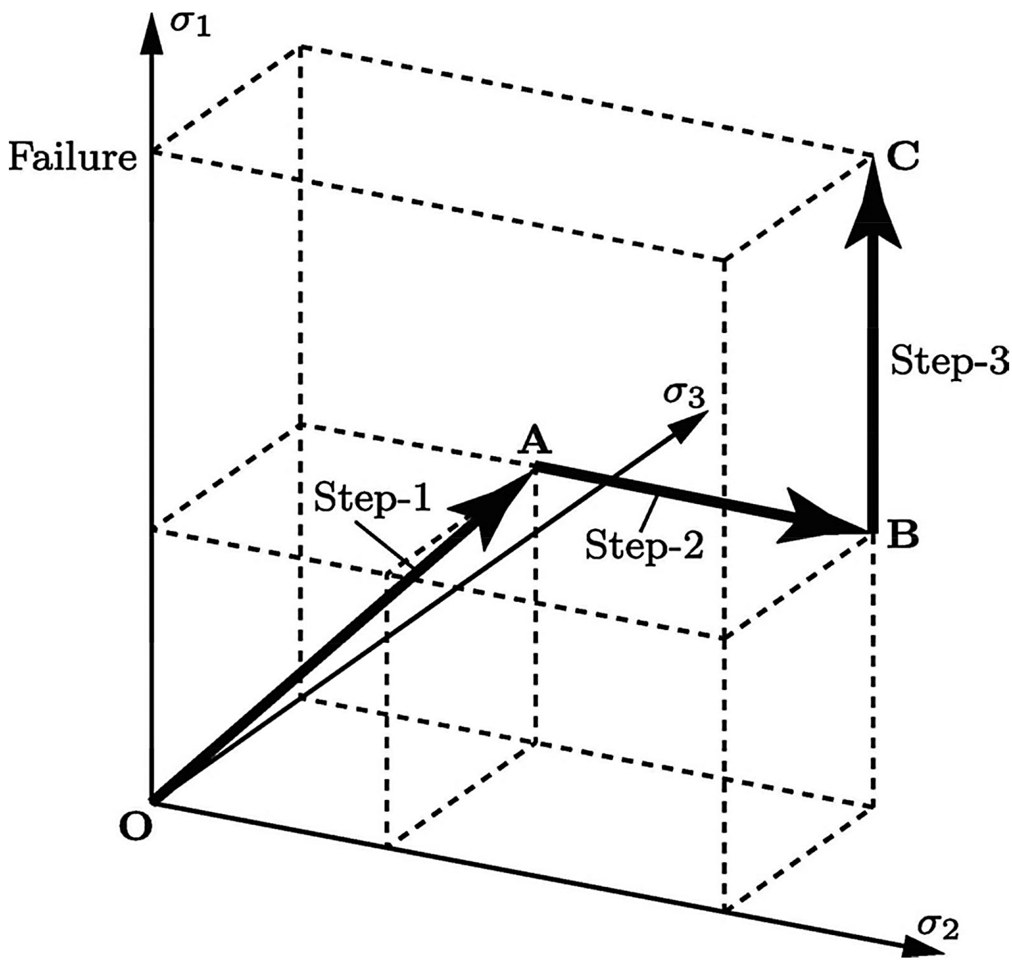

Figure 5. Loading path of the true triaxial tests before specimen failure. The permeability is measured in the third step.

centering device could be lowered to allow the specimen to deform freely.

(3) Exertion of the confining pressure and pore pressure

The triaxial vessel was filled with hydraulic oil, and the confining pressure was increased to the predetermined value at a rate of 0.1 MPa/s. The temperature of the hydraulic oil and thermostat tank that accommodated the TPM-6 was increased to 303 K. To ensure that no other fluid was in the system, all the lines and specimens were evacuated for more than 30 min at a vacuum manometer reading higher than 9.9. The valve of syringe pump 1 was opened to increase the system pressure to the predetermined pore pressure and maintain the constant pressure mode of the pump.

(4) True triaxial loading and permeability measurement

Figure 5 shows the loading path during true triaxial compression. Because the confining pressure (Step 1) had already been applied, the loading of the specimen started at Step 2. Therefore, the load in the σ_2 direction was initially increased to a constant value at a rate of 0.1 MPa/s and then held constant during subsequent loading. The loading of σ_1 in Step 3 was initially controlled at a stress rate of 0.1 MPa/s. As ε_3, which is the strain in the σ_3 direction, approached 4 $\mu\varepsilon$/s, the loading control of σ_1 was switched to a constant ε_3 rate of 4 $\mu\varepsilon$/s. During loading in Step 3, the permeability in the σ_2 direction, k_2, was measured at different strain states. During the tests of the permeability at one stress state, a pulse pressure of 150 kPa was applied by syringe pump 1, and the permeability measurement at this state was stopped when ΔP had decayed by more than 50%. Moreover, the permeability variation is directly related to the strains, which reflect the change in the structures of the pores and cracks of the specimen; therefore, the strain ε_3 (controlling target) other than σ_1 was maintained during each of the permeability tests.

(5) Completion of the test

The compression of the specimen ended when σ_1 reached the residual strength of the specimen. The σ_1, σ_2, pore pressure and confining pressure were sequentially unloaded to zero. The tests were also stopped when ε_1 exceeded 8% because the spacers of σ_2 are 9 mm shorter than the specimen, and continuous deformation will cause conflicts between the σ_1 spacers and the σ_2 spacers.

Repeatability tests

Repeatability tests were performed on unmentioned specimen P5 at stress states of 65, 17, and 15 MPa with a pore pressure of 5 MPa. As shown in Fig. 6(a), the relative standard deviation (RSD) of the ten permeabilities obtained from the repeatability test is 2.46%, which shows that the subsystem for measuring the permeability is stable. Figure 6(b) shows that the natural logarithm of the differential pressure ΔP associated with the first measurement decreases linearly over time. The stability and accuracy of the other subsystems of the TTA for the loading of the three principal stresses were also demonstrated by Shi *et al.*[31]

Results

Figures 7 and 8 show the deformation behavior and permeability evolution at confining pressures of 8 and 35 MPa, respectively. The permeability and mechanical behaviors observed in the tests are provided in Tables 1 and 2, respectively.

Specimens P4 and P15 were compressed at a low value of σ_2 (i.e., $\sigma_2 \approx \sigma_3$), which means that they were compressed under conventional triaxial stress conditions. A comparison of the results shown in Figs 7 and 8(a) illustrates that the confining pressure has a significant impact on the change in permeability of the specimen under compression. The maximum permeability $k_{2\max}$ of P4 at a confining pressure of 8 MPa increased by more than 400 times relative to k_{2a}, which is the permeability measured at the beginning of σ_1 loading. However, when the confining pressure was

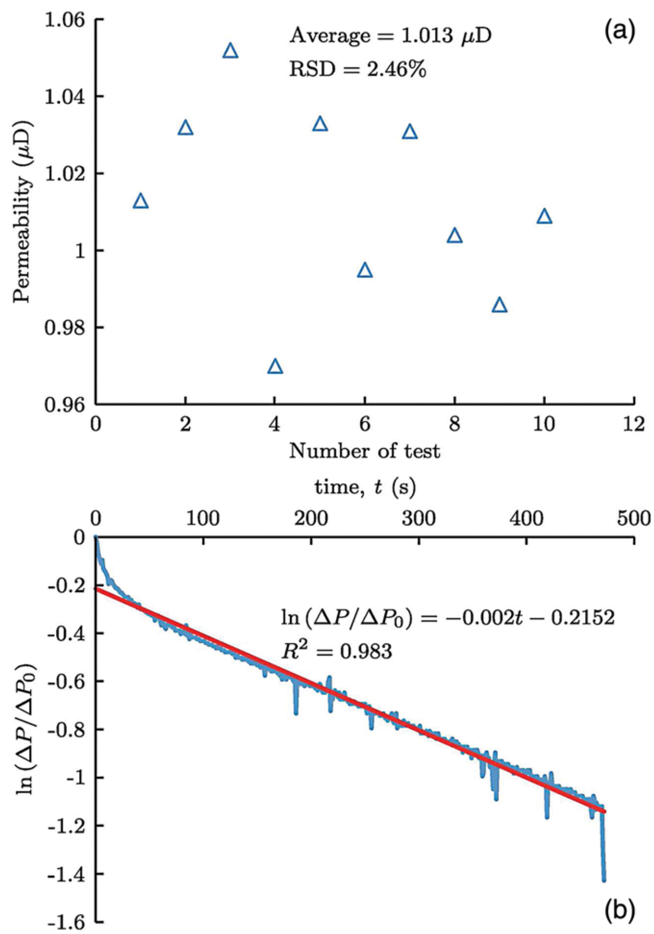

Figure 6. Repeatability tests: (a) permeabilities obtained from ten measurements and (b) decay curve of the differential pressure in the first measurement.

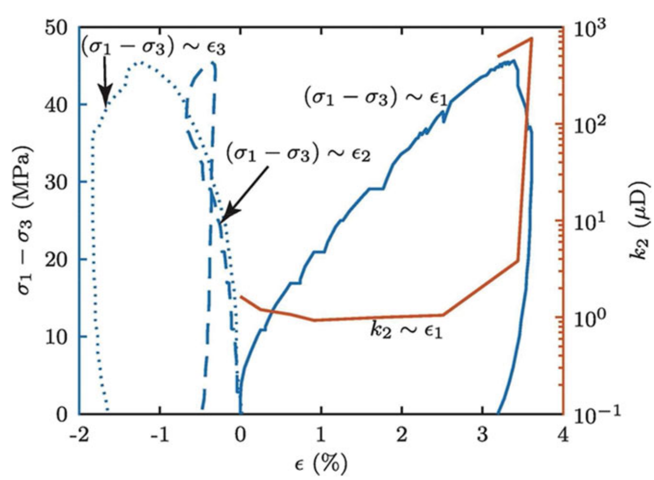

Figure 7. Deformation behavior and permeability evolution during true triaxial compression with σ_2, σ_3 and P_0 held at 10 MPa, 8 MPa, and 5 MPa, respectively.

Table 1. Permeability test results.

Specimen	Confining pressure σ_3 (MPa)	Intermediate principal stress σ_2 (MPa)	Pore pressure P_0 (MPa)	Initial permeability k_{2a} (μD)	Minimum permeability k_{2min} (μD)	Maximum permeability k_{2max} (μD)	Ratio of k_{2max} to k_{2a}
P4	8	10	5	1.64	0.93	763.47	465
P15	35	36	15	1.25	0.50	1.25	1
P11	35	41	15	1.16	0.77	3.37	2.92
P14	35	50	15	0.75	0.46	2.35	3.12
P16	35	60	15	0.40	0.24	1.46	3.63

Table 2. Mechanical behavior test results.

Specimen	ε_1 at failure ε_{1f} (%)	ε_2 at failure ε_{2f} (%)	ε_3 at failure ε_{3f} (%)	ε_v at failure ε_{vf} (%)	Deformation modulus E (GPa)	Strength (MPa)	Residual strength (MPa)	Degree of ductility ε_d (%)
P4	3.39	−0.37	−1.83	−1.19	1.86	86.28	44.80	1.16
P15	8.01	−2.74	−3.40	1.87	2.46	129.43	/	4.17
P11	5.40	−1.55	−1.89	1.98	3.52	134.77	105.89	2.57
P14	4.22	−0.43	−1.66	2.13	3.81	126.36	103.57	1.82
P16	3.37	−0.12	−1.20	2.06	5.07	133.39	103.69	1.43

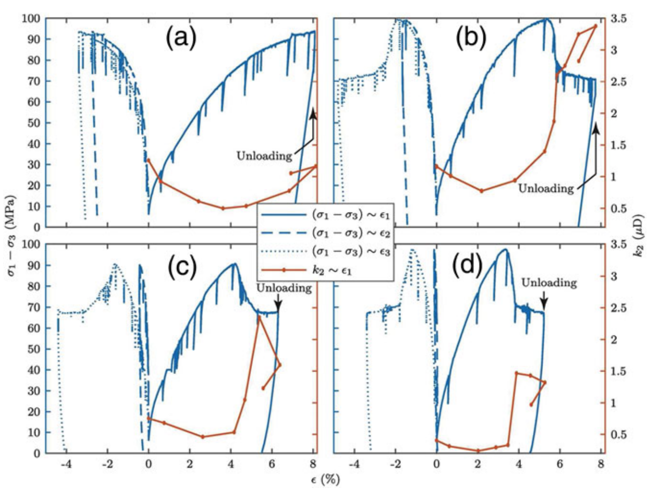

Figure 8. Deformation behavior and permeability evolution during true triaxial compression at different σ_2 values with σ_3 held at 35 MPa and P_0 equal to 15 MPa. The intermediate principal stresses of (a), (b), (c), and (d) were held at 36, 41, 50, and 60 MPa, respectively.

increased to 35 MPa, the ratio of k_{2max} to k_{2a} was equal to 1.

As shown in Fig. 8, the mechanical behavior and permeability under the compression conditions are also related to the magnitude of σ_2 as follows:

(1) Effect of σ_2 on the strength

Although many true triaxial compressive tests have demonstrated that the strength of rocks can be increased by increasing σ_2,[25–27] the strength of this mudstone was not affected, which is illustrated by the 6% relative difference between the maximum and minimum strengths. The effect may be weak and unobservable because of the dispersion of the results. The residual strengths of P11, P14, and P15 are also very similar. Although the strengths of the specimens at different values of σ_2 are highly similar, the difference between the permeability evolutions is notable. Thus, there is no direct correlation between the permeability and the stress state.

(2) Effect of σ_2 on the deformation behavior

The ductility of the mudstone, which increases considerably with increasing confining pressure, decreases notably due to the increase in σ_2. As σ_2 increases from 36 MPa to 60 MPa, ε_1 at catastrophic failure decreases by approximately 60%. In addition, ε_2 and ε_3 at failure are significantly reduced. To describe the ductility more quantitatively, the degree of ductility is defined according to Handin[38] as

$$\epsilon_d = \epsilon_{1f} - \frac{(\sigma_1 - \sigma_3)_f}{E} \qquad (2)$$

where ε_{1f} is the strain ε_1 at failure; $(\sigma_1 - \sigma_3)_f$ is the deviatoric stress in the σ_1 direction at failure (i.e., the

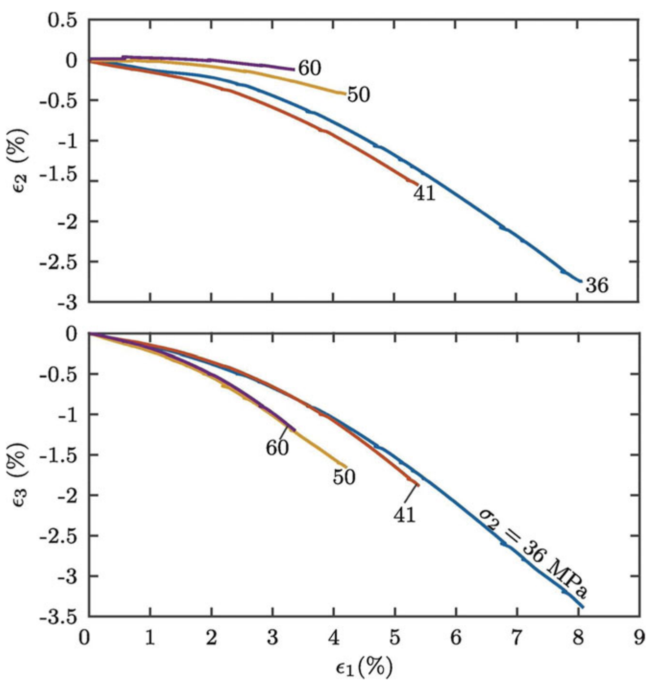

Figure 9. Comparison of strains ε_2 and ε_3 as functions of ε_1 in the mudstone. The numerals near the curves are the σ_2 values in MPa.

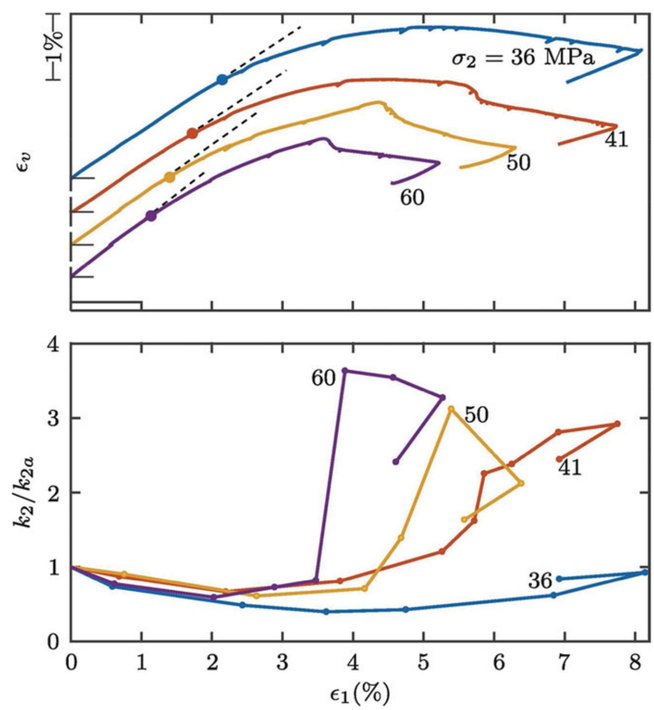

Figure 10. Volumetric strain ε_v and permeability k_2 as functions of ε_1 for the Yingcheng mudstone; the variation in permeability is normalized. The numerals for each curve are the σ_2 values in MPa.

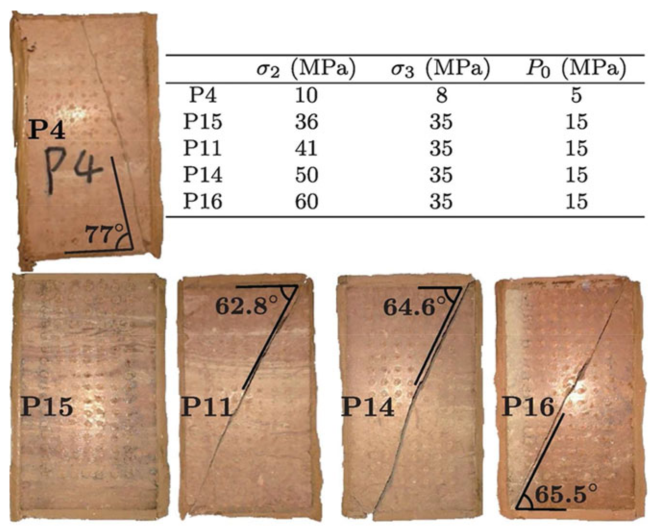

	σ_2 (MPa)	σ_3 (MPa)	P_0 (MPa)
P4	10	8	5
P15	36	35	15
P11	41	35	15
P14	50	35	15
P16	60	35	15

Figure 11. Photographs showing the failures of the mudstone specimens in the σ_2 direction.

difference between the strength and σ_3); and E is the deformation modulus. Therefore, ε_d is the actual permanent strain in the σ_1 direction before failure. Based on the ε_d value of each specimen (Table 2), the failure mode of P15 can be classified as semi-brittle, which is defined as failure at a ε_d value between 3% and 5%.[39] With increasing σ_2, ε_d decreases gradually, and the failure mode of the mudstone transitions from semi-brittle to brittle with increasing σ_2.

As shown in Fig. 9, at low σ_2 values of 36 and 41 MPa, the strains ε_2 and ε_3 approach each other and increase considerably before the failure of the specimen. As σ_2 is increased to 60 MPa, ε_3 increases considerably, whereas ε_2 increases nearly linearly with ε_1. This result indicates that the mudstone specimens exhibit dilatancy of directivity under true triaxial compression and that the dilatancy in the σ_3 direction is dominant, particularly when σ_2 is relatively high.

The volumetric strain ε_v is plotted against ε_1 in Fig. 10. The volumetric strain initially decreases linearly, which means that the specimen is in an elastic state. Dilatancy occurs in the specimen as the curve deviates from the linear segment. The results show that ε_1 at the onset of dilatancy increases with increasing σ_2. In addition, an interesting phenomenon is that the volumetric strains of all the specimens under different σ_2 values are similar at failure.

(3) Effect of σ_2 on fault formation

As shown in Fig. 11, all the specimens failed on a nearly flat plane, except P15, which did not reach

  | *Greenhouse Gas Sci Technol*. **8**:37–50 (2018); DOI: 10.1002/ghg

failure because of the high ductility of the mudstone at relatively high confining pressures. The fracture angle, which is the angle between the normal of the fault plane and the σ_1 direction, decreased markedly with increasing σ_3. As the confining pressure increased from 8 MPa to 35 MPa, the fracture angle decreased by more than 10°. Moreover, as σ_3 remained constant, the fracture angle was also correlated with σ_2. The fracture angle increased slightly from 62.8° to 65.5° as σ_2 increased from 41 to 60 MPa. Overall, the formation of the fault and the fracture angle are closely related to the deformation mechanism of the mudstone, which is also influenced by σ_2 and σ_3.

(4) Permeability change

In general, the evolution of the permeability of mudstone under true triaxial compression with shear faulting exhibits four stages. Initially, the closure of microcracks and the collapse of the pores causes a decrease in k_2. When the specimen is deformed plastically, the microcracks in the specimen begin to propagate, which causes the permeability to increase gradually until reaching the peak, and the permeability is higher when the $(\sigma_1 - \sigma_3) - \varepsilon_1$ curve deviates more from a straight line. Figure 10 shows comparisons of the variations of k_2 and ε_v with ε_1. The change in k_2 in the first two stages before the peak is the result of the combined effects of compaction and dilatancy. When the specimen begins to exhibit dilatancy, the compaction process continues. Therefore, the inflection point of the curve of k_2 vs. ε_1 appears after the onset of dilatancy. In the post-peak region, a decrease in stress is associated with the formation of the fault. The change in permeability accompanied by a sharp increase marks the beginning of the third stage. The fault will then slip with increasing ε_1, and two factors will lead to the uncertainty of the variation of k_2: shear dilatancy and the formation of debris. The appearance of the faults is shown in Fig. 11. The fault in P16 is relatively flat and is not conducive to shear dilatancy and the formation of debris. Therefore, its permeability does not change considerably in the fourth stage. However, the permeabilities of P11 and P14 increase and decrease, respectively.

In the initial portion of Step 3, the permeability of the mudstone k_{2a} decreases with increasing σ_2, which is well understood because the specimen is in the elastic phase, and a larger σ_2 makes the specimen more compact. Furthermore, the minimum permeability under compression $k_{2\min}$ and the permeability at failure are negatively correlated with σ_2; that is, a higher σ_2 is useful for the sealing performance of mudstone caprock in terms of the permeability before failure. In the post-peak region, as shown in the bottom portion of Fig. 10, the ratio of the maximum permeability $k_{2\max}$ to k_{2a} increases notably with increasing σ_2. However, because k_{2a} is lower at a higher σ_2, $k_{2\max}$ decreases with increasing σ_2.

In general, the effect of the confining pressure on the permeability is significantly greater than that of σ_2; however, the mudstone becomes more brittle with increasing σ_2, which causes a reduction in the deformation that is required for a sharp increase in the permeability.

Discussion

The fundamental reasons for the evolution of the permeability of mudstone are the change in its microstructure in the pre-peak stage, the formation of the fault, and the shear displacement of the fault in the post-peak stage.[40] Below, we discuss the permeability evolution and the deformation mechanism in terms of these aspects.

Mechanism of the effect of σ_2 on the permeability before failure

The grains of mudstone are extremely fine and contain many platy or rod-shaped clay minerals. Under triaxial compression conditions, mudstone grains tend to rearrange and align to make the mudstone denser. In addition, mudstone contains many microcracks,[35,41] which provide channels for the flow with the pores and are easily closed under compression. Therefore, the permeability of mudstone during non-dilatant deformation is generally more sensitive to the stress than that of sandstone, as was demonstrated by an experimental comparison of the evolution of permeability of the Dangyang mudstone and Ordos sandstone with increasing effective hydrostatic pressure.[41] Consider a stress sensitivity coefficient of permeability a as

$$a = \frac{\mathrm{d}\log\frac{k_2}{k_{2i}}}{\mathrm{d}\sigma} \tag{3}$$

where σ is the stress in MPa, and k_{2i} is the apparent permeability, which is not the real initial value. The average value of a of the mudstone under a confining pressure of 35 MPa as σ_2 increases from 36 to 50 MPa is 0.049, whereas that of the Kimachi Sandstone, as tested by Li[11], is between 1×10^{-3} and 2×10^{-3}. When calculating the value of a of the mudstone, σ_1 equals 35 MPa. Therefore, increasing σ_2 before the onset of dilatancy can increase the degree of closure of the microcracks, which increases the normal stresses and causes the permeability to decrease further.

In contrast to the closure of the microcracks, when σ_1 exceeds a certain value, the microcracks begin to initiate, reopen, and propagate, which will increase the permeability of the mudstone. As noted above, the mudstone exhibits so-called anisotropic dilatancy. When $\sigma_2 = 36$ MPa, the ε_1 values at the onset of dilatancy in the σ_2 and σ_3 directions are 1.387% and 1.458%, respectively, and the corresponding σ_1 values are 39.77 and 40.84 MPa, respectively. The dilatancies in the two directions are approximately equal. As σ_2 increases to 60 MPa, the onset of dilatancy in the σ_2 direction occurs at $\varepsilon_1 = 1.115\%$ and $\sigma_1 = 54.11$ MPa, whereas the onset of dilatancy in the σ_3 direction occurs at $\varepsilon_1 = 2.099\%$ and $\sigma_1 = 79.15$ MPa. These results show that σ_2 greatly hinders the propagation of the microcracks in the σ_2 direction. Even in the dilatant deformation stage before failure, the permeability at a constant σ_1 decreases with increasing σ_2. In addition, increasing σ_2 causes both the σ_1 at which the dilatancy initially occurs and the σ_1 that corresponds to the turning point of the change in permeability under compression to increase.

Many permeability functions based on stress, strain and damage have been proposed to describe the evolution of permeability.[42–45] These models use a segmentation function or a damage threshold to reflect the variation in permeability, which initially increases and then decreases during compression. Additionally, the damage parameter cannot be measured directly in the tests. Because the change in permeability is directly related to the compressive deformation ε_1 and the dilatant deformations in the σ_3 direction, we can assume that its evolution follows

$$k_2 = k_{2a}\left(e^{-\alpha\varepsilon_1} + \beta r_d^3\right) \quad (4)$$

where r_d is a ratio that represents the weight of the dilatant deformation in the σ_3 direction and can be calculated as shown in Fig. 12; and α and β are factors that reflect the effects of ε_1 and r_d on the permeability, respectively. The parameters α and β were set to 29.7 and 4.109, respectively, in this paper. With these two parameters, the numerical and experimental permeabilities are plotted in Fig. 13, which shows good consistency between the numerical results and

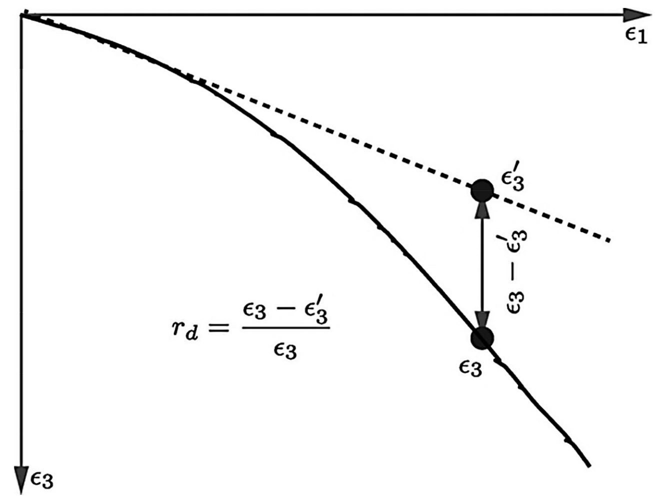

Figure 12. Diagram for calculating the amount of the dilatant deformation r_d.

experimental data, except for specimen P11 at a σ_2 of 41 MPa. We cannot expect this function to be highly accurate in predicting changes in permeability because there is heterogeneity between the specimens, and the function is simplified such that ε_2 is not considered. However, Eqn (4) captures the dominant factors in the changes in permeability under compression and is useful in practice. Although σ_2 has a considerable influence on the strains before failure, it has only a slight effect on α and β, which can reflect the relative change in the mudstone permeability.

The important effect of σ_2 is that the ductile deformation of the mudstone before failure is weakened by increasing σ_2, which likely occurs because grain sliding is impeded considerably. In fluid injection projects, ductile rock does not fail easily because (1) the larger deformation is beneficial for the attenuation of the fluid pressure and (2) the other two directions require greater stress increases to prevent deformation. Therefore, this σ_2 effect is detrimental for maintaining the integrity of mudstone caprock.

Mechanism of the effect of σ_2 on permeability after failure

Many conventional triaxial tests[11,46,47] have shown that rock specimens fracture with a highly uneven plane even though the confining pressure is greater than 20 MPa. However, specimens compressed by Mogi-type TTAs always manifest a fracture pattern of shearing on a planar fault that is parallel to σ_2. In the stress state of $\sigma_2 = \sigma_3$, microcracks with the same dip angle have an

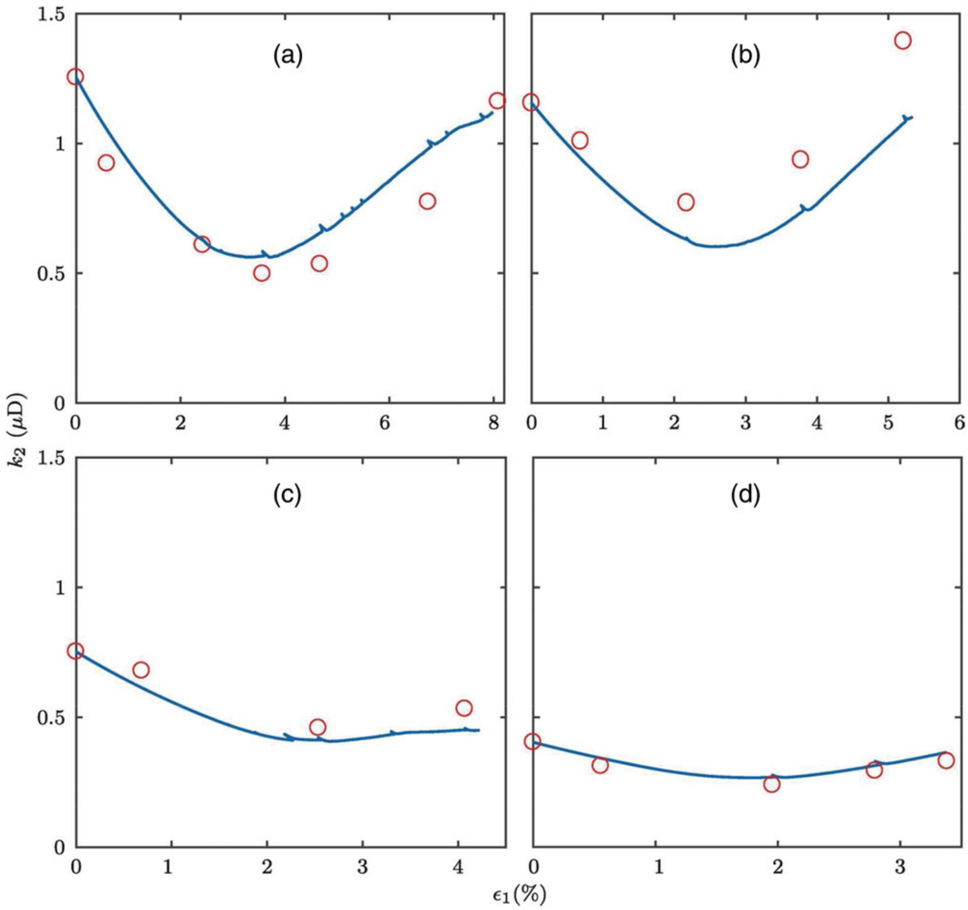

Figure 13. Comparison of the experimental data (circles) and numerical results (lines) of the permeability evolution at different σ_2 values of 36, 41, 50, and 60 MPa in (a), (b), (c), and (d), respectively.

equal probability of propagating, and the final fault may form by the random coalescence of these microcracks. As noted above, propagation of the microcracks toward the σ_2 direction is prevented by increasing σ_2, which is revealed by numerical tests.[48] In addition, the axial splitting or shear propagation of microcracks parallel to the σ_2 direction can be accelerated because the in-plane load of σ_2 can increase the stress intensity factor and reduce the normal stress on the microcracks.[49] Thus, faults that form under conditions of $\sigma_2 > \sigma_3$ are flatter than those that form at $\sigma_2 = \sigma_3$, and the roughness of the fault generally decreases with increasing σ_2, as is illustrated by the failure of Dunham dolomite,[26] Baoxing marble[31] and the mudstone considered in this paper. Moreover, the fault forms due to a combination of axial splitting and shear failure of the microcracks, and the combined effects of σ_1 and σ_2 will cause more microcracks that are perpendicular to the σ_3 direction to split, which is why the fault becomes slightly steeper (Fig. 11) with increasing σ_2.

The fault zone in the mudstone in the Koetoi Formation reported by Uehara and Takahashi[40] is denser and less permeable than the host rock because the rock can yield with pore collapse at a hydrostatic stress of 10 MPa. However, the phenomenon of yielding at the hydrostatic stress was not observed in the Yingcheng mudstone. Therefore, during fault formation in the Yingcheng mudstone, there is a corresponding sudden increase in the permeability in the tests because the fault can be an effective flow path. The fault may link the leaky bed and other primary faults within the caprock to form a tortuous but effective leakage path.[20] In general, the fault is quite permeable under low confining pressures due to its unevenness because the fault can dilate more easily. At high confining pressures, a compacting shear fault is formed. The permeability of the mudstone increases by only 1 to 2 μD from the peak at an effective confining pressure of 20 MPa.

The increase in permeability due to the formation of the fault in specimens at σ_2 values of 41, 50 and 60 MPa are 1.98, 1.81, and 1.14 μD, respectively, which indicates that the flow conductivity of the fault is also positively correlated with its roughness, which, as noted above, decreases with increasing σ_2. In addition, with shear displacement, a rougher fault will produce more debris to fill the opened part of the fault, which in turn increases the reduction of the permeability.

Conclusions

We conducted laboratory experiments to investigate the effect of the intermediate principal stress on the change in the permeability of the Yingcheng mudstone under true triaxial compression. To simulate the conditions of a caprock in a CCS project, the confining pressure and pore pressure were set to 35 and 15 MPa, respectively. In addition, the compression-induced variation in permeability of the mudstone at low confining pressures was examined as a comparison. The main conclusions of the study are as follows:

(1) The ductility of the mudstone decreases significantly with increasing intermediate principal stress. This reduced ductility has a detrimental effect on the integrity of the caprock because the brittle mudstone is more susceptible to failure with a constant strength.

(2) A greater intermediate principal stress reduces the permeability under compression.

(3) An empirical equation is proposed to describe the relative variation in permeability before the peak. The equation can accurately predict the permeability during compressive deformation and dilatant deformation of the specimen. The intermediate principal stress has only a slight influence on the parameters of the equation even though the strains in three directions change significantly.

(4) The specimen failed with a nearly flat fault that is parallel to the intermediate principal stress. A greater intermediate principal stress leads to a lower roughness of the fault. The rapid increase in the specimen permeability is directly related to the formation of the fault; however, the increase is only 1 to 2 μD under a high confining pressure, which is considerably smaller than that under a low confining pressure. The fluid conductivity of the fault is also influenced by its roughness. Therefore, the increase in permeability due to the fault is indirectly influenced by the intermediate principal stress.

In summary, except for inducing a significant reduction in the ductility of the mudstone, the intermediate principal stress has a smaller effect on the permeability of the mudstone than the confining pressure. However, the sudden increase of the permeability by a factor of 2–3 that is accompanied by the formation of the fault due to the decrease in ductility caused by the increase of the intermediate principal stress cannot be neglected in the evaluation of CCS leakage over geological time. This understanding of the effect of the intermediate principal stress on the permeability change is preliminary because the relevant experiments were completed at a high confining pressure. In future work, we will conduct experiments at different pore pressures to understand this effect more comprehensively.

Acknowledgements

The authors acknowledge financial support from the National Natural Science Foundation of China under Grants No. 11102220 and No. 41172285.

References

1. IPCC, *Carbon Dioxide Capture and Storage*. *Intergovernmental Panel on Climate Change*. WMO & UNEP, Cambridge University Press, New York (2005).
2. Holloway S, An overview of the underground disposal of carbon dioxide. *Energy Convers Manage* **38**:S193–S198 (1997).
3. Bachu S, CO_2 storage in geological media: Role, means, status and barriers to deployment. *Prog Energ Combust Sci* **34**:254–73 (2008).
4. Bai B, Li X, Wu H, Wang Y and Liu M, A methodology for designing maximum allowable wellhead pressure for CO2 injection: application to the Shenhua CCS demonstration project, China. *Greenh Gases Sci Technol* **7**(1):158–181 (2017).
5. Li Q, Wu Z, Li X, Ohsumi T and Koide H, Numerical simulation on crust deformation due to CO_2 sequestration in deep aquifers. *J Appl Mech* **5**:591–600 (2002).
6. Li X, Liu Y, Bai B and Fang Z, Ranking and screening of CO_2 saline aquifer storage zone in China. *Chinese J Rock Mech Eng* **25**(5):963–968 (2006).
7. Benson SM and Cole DR, CO_2 sequestration in deep sedimentary formations. *Elements* **4**(5):325–331 (2008).
8. Li X, Manabu T, Wu Z, Koide H and Ohsumi T, Faulting-induced permeability change in Shirahama Sandstone and implication for CO_2 aquifer storage. *Chinese J Rock Mech Eng* **22**(6):995–1001 (2003).

9. Li X, Koide H and Ohsumi T, CO_2 aquifer storage and the related rock mechanics issues. *Chinese J Rock Mech Eng* **22**(6):989–994 (2003).
10. Brace WF, A note on permeability changes in geologic material due to stress. *Pure Appl Geophys* **116**(4):627–33 (1978).
11. Li X, Permeability Change in Sandstones under Compressive Stress C*ondition*. Ibaraki University, Ibaraki (2001).
12. Jiang Z and Ji L, The laboratory study on behavior of permeability of rock along the complete stress-strain path. *Chinese J Geotech Eng* **23**(2):153–156 (2001).
13. Wang JA and Park HD, Fluid permeability of sedimentary rocks in a complete stress-strain process. *Eng Geol* **63**(3–4):291–300 (2002).
14. Zhang J, Standifird WB, Roegiers JC and Zhang Y, Stress-dependent fluid flow and permeability in fractured media: From lab experiments to engineering applications. *Rock Mech Rock Eng* **40**(1):3–21 (2007).
15. Chen L, Liu JF, Wang CP, Liu J, Su R and Wang J, Characterization of damage evolution in granite under compressive stress condition and its effect on permeability. *Int J Rock Mech Min Sci* **71**:340–349 (2014).
16. Torp TA and Gale J, Demonstrating storage of CO_2 in geological reservoirs: The Sleipner and SACS projects. *Energy* **29**(9–10):1361–1369 (2004).
17. Underschultz J, Boreham C, Dance T, Stalker L, Freifeld B, Kirste D *et al*., CO_2 storage in a depleted gas field: An overview of the CO2CRC Otway Project and initial results. *Int J Greenh Gas Control* **5**(4):922–932 (2011).
18. Rutqvist J, The geomechanics of CO_2 storage in deep sedimentary formations. *Geotech Geol Eng* **30**(3):525–551 (2012).
19. Wu X, Shenhua Group's carbon capture and storage (CCS) demonstration. *Min Rep* **150**(1–2):81–84 (2014).
20. Ingram GM and Urai JL, Top-seal leakage through faults and fractures: the role of mudrock properties. *Geol Soc London, Spec Publ* **158**(1):125–135 (1999).
21. Brown ET and Hoek E, Trends in relationships between measured in-situ stresses and depth. *Int J Rock Mech Min Sci Geomech Abstr* **15**(4):211–215 (1978).
22. Haimson BC, The hydrofracturing stress measuring method and recent field results. *Int J Rock Mech Min Sci Geomech Abstr* **15**(4):167–178 (1978).
23. Mcgarr A and Gay NC, State of stress in earth's crust. *Annu Rev Earth Planet Sci* **6**:405–436 (1978).
24. Jing F, Sheng Q, Zhang Y, Luo C and Liu Y, Research on distribution rule of shallow crustal geostress in China mainland. *Chinese J Rock Mech Eng* **26**(10):2056–2062 (2007).
25. Haimson B and Chang C, A new true triaxial cell for testing mechanical properties of rock, and its use to determine rock strength and deformability of Westerly granite. *Int J Rock Mech Min Sci* **37**(1–2):285–296 (2000).
26. Mogi K, *Experimental Rock Mechanics*. Taylor & Francis, Leiden AK (2007).
27. Feng X, Zhang X, Kong R and Wang G, A novel Mogi type true triaxial testing apparatus and its use to obtain complete stress-strain curves of hard rocks. *Rock Mech Rock Eng* **49**(5):1649–1462 (2016).
28. Takahashi M, Sugita Y, Xue Z, Oonishi Y and Ishijima Y, Three principal stress effects on permeability of the Shirahama Sandstone: in case of stress state prior to dilatancy. *J MMIJ* **109**(10):803–809 (1993).
29. Al-Harthy SS, Jing XD, Marsden JR and Dennis JW, Petrophysical properties of sandstones under true triaxial stresses I: directional transport characteristics and pore volume change. In SPE Asia Pacific Improved Oil Recovery Conference, October 25–26, Kuala Lumpur, SPE 57287 (1999).
30. Li X, Shi L, Bai B, Li Q, Xu D and Feng X, True-triaxial testing techniques for rocks: State of the art and future perspectives. In *Proceedings of TTT workshop*, 17 Oct, CRC Press/Balkema, Leiden AK, pp. 3–18 (2011).
31. Shi L, Li X, Wang A, Zeng Z and He H, A Mogi-type true triaxial testing apparatus for rocks with two moveable frames in horizontal layout for providing orthogonal loads. *Geotech Test J* **40**(4):542–558 (2017).
32. Hu S, Li X, Bai B, Shi L, Liu M and Wu H, A modified true triaxial apparatus for measuring mechanical properties of sandstone coupled with CO_2-H_2O biphase fluid. *Greenh Gases Sci Technol* **7**(1):78–91 (2017).
33. Li X, Wang Y and Wei N, Research on measuring method of permeability by using storage-variable transient pulse method. *Chinese J Rock Mech Eng* **27**(12):2482–2487 (2008).
34. Wang Y, Li X and Wei N, Experimental study of storage-variable transient pulse method for permeability measurement. *Chinese J Rock Mech Eng* **29**(S1):3113–3121 (2010).
35. Zeng Z, Li X, Shi L, Bai B, Fang Z and Wang Y, Experimental study of the laws between the effective confining pressure and mudstone permeability. *Energy Procedia* **63**:5654–5663 (2014).
36. Brace WF, Walsh JB and Frangos WT, Permeability of granite under high pressure. *J Geophys Res* **73**(6):2225–2236 (1968).
37. Jones SC, A technique for faster pulse-decay permeability measurements in tight rocks. *SPE Formation Evaluation* **12**(1):19–25 (1997).
38. Handin J, Strength and ductility. *GSA Memories* **97**:223–290 (1966).
39. Evans B, Fredrich JT and Wong TF, The brittle-ductile transition in rocks: recent experimental and theoretical progress. In: *The Brittle-Ductile Transition in Rocks*. American Geophysical Union, Washington, DC, pp. 1–20 (2013).
40. Uehara S and Takahashi M, Evolution of permeability and microstructure of experimentally-created shear zones in Neogene siliceous mudstones from Horonobe, Japan. *J Struct Geol* **60**:46–54 (2014).
41. Zeng Z, Li X, Shi L and Bai B, Testing study on variational characteristics of the permeability for mudstone and sandstone with the change of confining pressure. *J Transp Sci Eng* **31**(4):1–5 (2015).
42. Tang CA, Tham LG, Lee PKK, Yang TH and Li LC, Coupled analysis of flow, stress, and damage (FSD) in rock failure. *Int J Rock Mech Min Sci* **39**(4):477–489 (2002).
43. Lyakhovsky V and Hamiel Y, Damage evolution and fluid flow in poroelastic rock. *Izv Phys Solid Earth* **43**(1):13–23 (2007).
44. Sun Q, Zhu S, Zhang R, Jiang C and Qian H, Analysis of permeability variation during the stress-strain process of rocks. *Goal Geol Explor* **40**(1):60–63 (2012).
45. Ma J. Review of permeability evolution model for fractured porous media. *J Rock Mech Geotech Eng* **7**(3):351–357 (2015).

46. Bésuelle P, Desrues J and Raynaud S, Experimental characterisation of the localisation phenomenon inside a Vosges sandstone in a triaxial cell. *Int J Rock Mech Min Sci* **37**(8):1223–1237 (2000).
47. Xia M and Zhou K, Particle simulation of the failure process of brittle rock under triaxial compression. *Int J Miner Metall Mater* **17**(5):507–513 (2010).
48. Deng S, Zheng Y and Yue C, Strength model and mesoscopic mechanism of intermediate principal stress effect on rock strength. *Sci Sin Technol* **47**(3):306–315 (2017).
49. Madenci E, Slightly open, penny-shaped crack in an infinite solid under biaxial compression. *Theor Appl Fract Mech* **16**:215–222 (1991).

Lu Shi

Lu Shi is an associate professor at the Institute of Rock and Soil Mechanics, CAS, China. He is mainly engaged in the development of rock true triaxial apparatus and the study of mechanics and permeability of rock under true triaxial stresses. In addition, he has also developed algorithms for numerical simulation in solid mechanics.

Zhijiao Zeng

Zhijiao Zeng is an assistant researcher at the Institute of Rock and Soil Mechanics, CAS, China. She focuses on the permeability evolution of rock materials under different loading paths. Dr Zeng has also been engaged in the development of permeability measurement equipment.

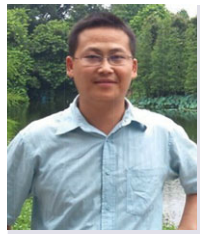

Bing Bai

Bing Bai is an associate professor at the Institute of Rock and Soil Mechanics, CAS, China. Since 2013, he has been engaged in the study of geomechanics relating to CO_2 storage and deep underground energy recovery. Representative achievements include the design methodology of CO_2 redline wellhead injection pressure of China Shenhua CCS pilot project. He is also the secretary of Theme 6, US-China Clean Energy Research Center on Advanced Coal Technology Consortium (CERC-ACTC 1.0).

Xiaochun Li

Xiaochun Li is a senior research scientist and research group leader at the Institute of Rock and Soil Mechanics, CAS, China. He is one of the pioneer scientists to introduce CCS into China. Li is engaged in research and development of CO_2 geological sequestration technology, and has made a series of vital achievements in interactions of rock failure and seepage, site selection, and mechanical stability.

  | *Greenhouse Gas Sci Technol*. **8**:37–50 (2018); DOI: 10.1002/ghg